Aalto University

OPEN ACCESS

This is an electronic reprint of the original article.
This reprint may differ from the original in pagination and typographic detail.

Kong, Beibei; Huang, Xiao Wei; Sheng, Xin Qing

A Discontinuous Galerkin Surface Integral Solution for Scattering from Homogeneous Objects with High Dielectric Constant

Published in:
IEEE Transactions on Antennas and Propagation

DOI:
10.1109/TAP.2019.2947139

Published: 01/01/2020

Document Version
Peer-reviewed accepted author manuscript, also known as Final accepted manuscript or Post-print

Please cite the original version:
Kong, B., Huang, X. W., & Sheng, X. Q. (2020). A Discontinuous Galerkin Surface Integral Solution for Scattering from Homogeneous Objects with High Dielectric Constant. *IEEE Transactions on Antennas and Propagation*, *68*(1), 598-603. Article 8876841. https://doi.org/10.1109/TAP.2019.2947139

This material is protected by copyright and other intellectual property rights, and duplication or sale of all or part of any of the repository collections is not permitted, except that material may be duplicated by you for your research use or educational purposes in electronic or print form. You must obtain permission for any other use. Electronic or print copies may not be offered, whether for sale or otherwise to anyone who is not an authorised user.

A Discontinuous Galerkin Surface Integral Solution for Scattering from Homogeneous Objects with High Dielectric Constant

Beibei Kong, Xiao-Wei Huang and Xin-Qing Sheng, *Senior Member, IEEE*

***Abstract*—The discontinuous Galerkin (DG) method for homogeneous bodies has been studied and shown to be an efficient tool for multi-scale homogeneous bodies. However, the slow convergence of DG with the block diagonal preconditioner (BDP) is still observed in solving high contrast homogeneous bodies. An efficient preconditioning approach is designed for the DG method in this communication by using the sparsing approach on the near-field matrix of the whole region. The iteration convergence speed of the DG method is improved while the computing resources for constructing the preconditioner are effectively reduced. Numerical experiments demonstrate the capability of the presented DG method for multi-scale homogeneous bodies, especially for those with a high dielectric constant.**

***Index Terms*—Discontinuous Galerkin method, homogeneous objects, high dielectric constant, multi-scale.**

I. Introduction

The domain decomposition method (DDM) is an attractive method in solving large multi-scale electromagnetic problems [1-5]. By decomposing the solution domain into several parts, the DDM can improve the flexibility, parallelism and the matrix convergence of the solution for complex simulation targets. In recent years, DDM has been extended to the method of moments [6-9]. In these methods, the whole solution region is partitioned into many sub-domains, and each sub-domain is described by a closed surface. The relation of these sub-domains is established by employing the equivalence principle [6, 7] or the Robin-type transmission condition (RTC) [8, 9]. Recently, a type of DDM called discontinuous Galerkin (DG) method has been successfully developed [10-13]. In the DG method, each sub-domain is not required to be enclosed by a closed surface. Fewer additional unknowns on the boundary of the sub-domains are needed, and the field relations on the interfaces between sub-domains in DG are intrinsically imbedded in the integral equation. The solution of DG with the surface integral equation (SIE) for non-penetrable objects has been well studied [10-11], and that for penetrable objects is presented in [12-14]. However, the slow convergence for DG with block diagonal preconditioner (BDP) is still observed in calculating homogeneous bodies with a high dielectric constant.

In this communication, we present a preconditioning approach for the DG solution of high dielectric constant homogeneous bodies, whose discretized matrix is very dense and difficult to converge. The Multilevel Fast Multipole Algorithm (MLFMA) is implemented in the solution. Numerical experiments are performed to investigate the performance of the proposed method on computational efficiency and resource consumption. The capability of the proposed DG solution is further validated for multi-scale homogeneous bodies.

This work was supported in part by the National Key Research and Development Program of China under Grant 2017YFB0202500 and in part by the NSFC under Grant U1730102.

B.-B. Kong, X.-W. Huang and X.-Q. Sheng are with the Center for Electromagnetic Simulation, Beijing Institute of Technology, Beijing 100081, China (corresponding author: X.-Q. Sheng, xsheng@bit.edu.cn). B.-B. Kong is currently a Postdoctoral researcher at the Department of Electronics and Nanoengineering, Aalto University.

II. Formulation

Consider electromagnetic scattering from a 3D homogeneous object, as illustrated in Fig. 1. The object is immersed in free space and illuminated by an incident plane wave ($\mathbf{E}^{\text{inc}}, \mathbf{H}^{\text{inc}}$). Let S represent the surface of the body. The interior region of the homogeneous object is denoted as Ω_2 and the exterior region is denoted as Ω_1. The permittivity and permeability of region Ω_l ($l = 1, 2$) are ε_l and μ_l, respectively. $\hat{\mathbf{n}}_l (l = 1, 2)$ denotes the unit normal of S pointing toward the interior of Ω_l. The equivalent electric and magnetic currents on the surface of the homogeneous body are denoted as $\mathbf{J}$ and $\mathbf{M}$, respectively.

The combined tangential field (CTF) equation is one of the stable surface integral formulations for the homogeneous scattering problem, which can be formulated as [14]

$$\mathbf{L}_1(\mathbf{J}) + \mathbf{L}_2(\mathbf{J}) - \frac{1}{Z_1}\mathbf{K}_1(\mathbf{M}) - \frac{1}{Z_2}\mathbf{K}_2(\mathbf{M}) = -\frac{1}{Z_1}\mathbf{E}^{\text{inc}} \tag{1}$$

$$\mathbf{L}_1(\mathbf{M}) + \mathbf{L}_2(\mathbf{M}) + Z_1\mathbf{K}_1(\mathbf{J}) + Z_2\mathbf{K}_2(\mathbf{J}) = -Z_1\mathbf{H}^{\text{inc}} \tag{2}$$

where $Z_l = \sqrt{\mu_l / \varepsilon_l}$, the integral-differential operators $\mathbf{L}_l$ and $\mathbf{K}_l$ are defined as follows:

$$\mathbf{L}_l(\mathbf{X}) = -jk_l \int \left[1 + \frac{1}{k_l^2}\nabla\nabla\cdot\right]\mathbf{X}(\mathbf{r}')G_l(\mathbf{r},\mathbf{r}')dS' \tag{3}$$

$$\mathbf{K}_l(\mathbf{X}) = -\int_{p.v.} \mathbf{X}(\mathbf{r}')\times\nabla G_l(\mathbf{r},\mathbf{r}')dS' + \frac{1}{2}\hat{\mathbf{n}}_i \times \mathbf{X} \tag{4}$$

where $G_l(\mathbf{r},\mathbf{r}') = e^{-jk_l|\mathbf{r}-\mathbf{r}'|}/\left(4\pi|\mathbf{r}-\mathbf{r}'|\right)$ with $k_l = \omega\sqrt{\varepsilon_l\mu_l}$ is the Green's function of region Ω_l, and *p.v.* stands for the principal value integral.

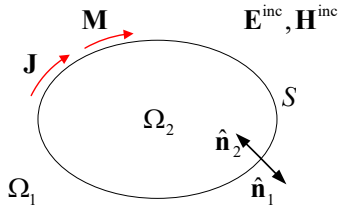

Fig. 1. The scattering from a 3D homogeneous target

We decompose the surface S into several non-overlapping sub-domains, as shown in Fig. 2 (a). Then, each

non-overlapping surface can be independently meshed by planar triangular patches. Let C denote the contour boundary between the adjacent subdomains. For the patches T_i $(i=1,2)$ on the side of the contour boundary between two different sub-domains, as shown in Fig. 2 (b), we denote the contour edge of patch T_i as C_i. Further, $\hat{\mathbf{t}}_i$ denotes the unit normal of C_i pointing toward the exterior of T_i.

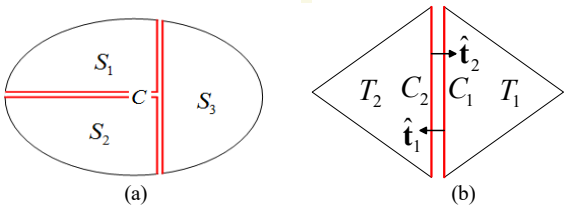

Fig. 2. (a) Non-overlapping decomposition for the surface of a homogeneous body. (b) Notations for the adjacent patches across the contour boundary.

In order to solve equations (1) and (2), the unknown surface currents $\mathbf{J}$ and $\mathbf{M}$ are approximated as the following linear combinations

$$\mathbf{J}=\sum_{i=1}^{N} J_i \mathbf{g}_i, \qquad \mathbf{M}=\sum_{i=1}^{N} M_i \mathbf{g}_i \tag{5}$$

where N is the total number of edges on S and $\mathbf{g}_i$ is the Rao–Wilton–Glisson (RWG) basis function for the currents inside the sub-domains or the half-RWG basis function [15] for the currents at the contour boundary. Using $\mathbf{g}_i$ as the testing function, we obtain the following discretized matrix equation

$$\begin{bmatrix} \mathbf{U} & \mathbf{Q} \\ \mathbf{R} & \mathbf{U} \end{bmatrix} \begin{bmatrix} J \\ M \end{bmatrix} = \begin{bmatrix} e \\ h \end{bmatrix} \tag{6}$$

where

$$\mathbf{U}_{ij}=\int_S \mathbf{g}_i \cdot [\mathbf{L}_1(\mathbf{g}_j)+\mathbf{L}_2(\mathbf{g}_j)]dS \tag{7}$$

$$\mathbf{Q}_{ij}=\int_S \mathbf{g}_i \cdot \left[-\frac{1}{Z_1}\mathbf{K}_1(\mathbf{g}_j)-\frac{1}{Z_2}\mathbf{K}_2(\mathbf{g}_j)\right]dS \tag{8}$$

$$\mathbf{R}_{ij}=\int_S \mathbf{g}_i \cdot \left[Z_1\mathbf{K}_1(\mathbf{g}_j)+Z_2\mathbf{K}_2(\mathbf{g}_j)\right]dS \tag{9}$$

$$e_i=-\frac{1}{Z_1}\int_S \mathbf{g}_i \cdot \mathbf{E}^{\text{inc}} dS, \qquad h_i=-Z_1\int_S \mathbf{g}_i \cdot \mathbf{H}^{\text{inc}} dS \tag{10}$$

For the hyper-singular integral in the operator $\mathbf{L}_l$, a common remedy is to transfer the double operators of ∇ to the basis and test functions respectively by using mathematical vector identities and integral theorems. The resulting line integral terms are canceled by the contribution of the adjacent RWG basis functions. However, in the domain decomposed case, the line integral terms on the contour boundary remain. The term with operator $\mathbf{L}_l(l=1,2)$ in (7) can be derived as [10]

$$\begin{aligned}\int_S \mathbf{g}_i \cdot \mathbf{L}_l(\mathbf{g}_j)dS &= -jk_l \int_S\int_{S'} \mathbf{g}_i \cdot \mathbf{g}_j G_l dS'dS \\ &+\frac{j}{k_l}\int_S \nabla\cdot\mathbf{g}_i \int_{S'} \nabla'\cdot\mathbf{g}_j G_l dS'dS - \frac{j}{k_l}\int_{C'} \hat{t}_j\cdot\mathbf{g}_j \int_S \nabla\cdot\mathbf{g}_i G_l dSdC' \\ &-\frac{j}{k_l}\int_C \hat{t}_i\cdot\mathbf{g}_i \int_{S'} \nabla'\cdot\mathbf{g}_j G_l dS'dC + \frac{j}{k_l}\int_C \hat{t}_i\cdot\mathbf{g}_i \int_{C'} \hat{t}_j\cdot\mathbf{g}_j G_l dC'dC\end{aligned} \tag{11}$$

According to the continuity of the current across the contour boundary, we have [10]

$$\hat{\mathbf{t}}_i\cdot\mathbf{X}_i+\hat{\mathbf{t}}_j\cdot\mathbf{X}_j=0 \quad on\ C_i,\ C_j \tag{12}$$

where C_i and C_j are the contour edges of the adjacent patches in different sub-domains. $\mathbf{X}_i$ represents the equivalent electric or magnetic current on C_i. Based on (12), the interior penalty terms can be derived as [10]

$$\sum_{C_i,C_j\in C}(\hat{\mathbf{t}}_i\cdot\mathbf{X}_i+\hat{\mathbf{t}}_j\cdot\mathbf{X}_j)=0 \tag{13}$$

$$\sum_{C_i,C_j\in C}\int_{C_j}(\hat{t}_i\cdot\mathbf{X}_i+\hat{t}_j\cdot\mathbf{X}_j)G_l dC'=0 \quad (l=1,2) \tag{14}$$

Discretizing the current in equation (13) and (14) with the half-RWG basis function and testing these two equations by $\hat{\mathbf{t}}_i\cdot\mathbf{g}_i$, the interior penalty stabilization terms can be linearly combined with the CTF discretized matrix equation (6). The final matrix equation of the DG method for dielectric bodies is expressed as

$$\begin{bmatrix} \mathbf{V} & \mathbf{Q} \\ \mathbf{R} & \mathbf{V} \end{bmatrix} \begin{bmatrix} J \\ M \end{bmatrix} = \begin{bmatrix} e \\ h \end{bmatrix} \tag{15}$$

where

$$\begin{aligned}\mathbf{V}_{ij}=&\sum_{l=1,2}[\mathbf{g}_i\cdot\mathbf{L}_l(\mathbf{g}_j)+\alpha\frac{j}{k_l}\int_C \hat{\mathbf{t}}_i\cdot\mathbf{g}_i\int_{C'}\hat{\mathbf{t}}_j\cdot\mathbf{g}_j G_l dC'dC \\ &+\beta\frac{j}{k_l}\int_{C_i}(\hat{\mathbf{t}}_i\cdot\mathbf{g}_i)(\hat{\mathbf{t}}_j\cdot\mathbf{g}_j)dC]\end{aligned} \tag{16}$$

Here α and β are arbitrary coefficients of the boundary penalty terms. Choosing α as -1, the term of the double contour integral in (11), which cannot be evaluated numerically when the field point approaches the source points, can be canceled. The optimum value of β will be investigated later. The MLFMA is implemented in the DG solution in order to speed up the computation of the matrix-vector multiplication.

III. Preconditioning Approaches

The above matrix (15) was found to convergence slowly. To obtain a linear system with a better iteration performance, a preconditioner is used to the matrix equation of (15), which yields

$$\mathbf{P}^{-1}\mathbf{M}x=\mathbf{P}^{-1}b \tag{17}$$

The DG method with block diagonal preconditioner (BDP) provides an efficient way to solve large multiscale homogeneous scattering problems [14]. However, we found that when the dielectric constant of some scatterers becomes large, the iteration convergence speed of the DG method seriously decreased. The numerical examples will be shown later. A more efficient preconditioning approach is needed for the DG method to solve the problem of high dielectric bodies.

Ignoring the decomposition of the target, we take the preconditioning approach for the whole matrix. We know from (6)-(9) that the value of $\mathbf{Q}$ is far less than that of $\mathbf{V}$ and $\mathbf{R}$. Hence, we use the lower triangular matrix as the preconditioning matrix $\mathbf{P}$. The inverse matrix $\mathbf{P}^{-1}$ can be directly obtained as

$$\mathbf{P}^{-1}=\begin{bmatrix}\mathbf{V}^{\mathrm{NF}} & 0\\ \mathbf{R}^{\mathrm{NF}} & \mathbf{V}^{\mathrm{NF}}\end{bmatrix}^{-1}=\begin{bmatrix}\left(\mathbf{V}^{\mathrm{NF}}\right)^{-1} & 0\\ -\left(\mathbf{V}^{\mathrm{NF}}\right)^{-1}\mathbf{R}^{\mathrm{NF}}\left(\mathbf{V}^{\mathrm{NF}}\right)^{-1} & \left(\mathbf{V}^{\mathrm{NF}}\right)^{-1}\end{bmatrix} \quad (18)$$

where $\mathbf{V}^{\mathrm{NF}}$ and $\mathbf{R}^{\mathrm{NF}}$ are the near-field matrices of MLFMA. This preconditioner is called the Lower Triangular Approximate Schur Preconditioner (LTASP) [16].

In the MLFMA solution for the surface integral formulation, the equivalent electric and magnetic currents on both sides of the surface share the same set of unknowns. In order to ensure the numerical accuracy, the box size of MLFMA is chosen according to the free space wavelength λ_0, while the mesh size of the target is chosen according to the medium wavelength $\lambda_0/\sqrt{\varepsilon_r}$. Thus, the number of unknowns N_0 in the lowest-level box of MLFMA is proportional to the dielectric constant ε_r. The number of the near-field elements is $O(N_0^2)$. When the dielectric of the scatterer is large, the near-field matrix will become very dense. Consequently, the LTASP is resource-consuming for the high dielectric bodies.

In our preconditioner construction, we extracted elements from the near-field lower triangular impedance matrix $\mathbf{P}$ to generate a sparse matrix, according to choice rule (19)

$$\mathbf{P}_{ij}^{\mathrm{sp}}=\begin{cases}\mathbf{P}_{ij} & |\boldsymbol{r}_i-\boldsymbol{r}_j|\le L\\ 0 & elsewhere\end{cases} \quad (19)$$

The interaction distance L of elements between source and field is chosen as the criterion to retain or omit the elements of $\mathbf{P}$. Thus, only the strong interactions are maintained in $\mathbf{P}^{\mathrm{sp}}$, especially the strong interactions from the contour boundary. The distance L is chosen according to the medium wavelength, as shown in (20)

$$L=a\lambda_0/\sqrt{\varepsilon_r} \quad (20)$$

where a is a constant. Note that the number of $\mathbf{P}^{\mathrm{sp}}$ is $O(N_0)$. The density of the preconditioning matrix is greatly reduced. We employ the inverse of $\mathbf{P}^{\mathrm{sp}}$ as a preconditioner and name it as distance sparse LTASP (DS-LTASP).

IV. Numerical Results

This section presents a series of numerical experiments, which were carried out to validate the accuracy and efficiency of the proposed approach. Our simulations use the generalized minimum residual (GMRES) solver with the dimension of the Krylov subspace of 100. The residual error is 10^{-3}, except for the experiments in Table II and Fig. 6, in which the residual error of GMRES is set to 10^{-5}. MUMPS is used to calculate the inverse of matrices. The computations are performed using a workstation with eight 14-core Intel(R) Xeon(R) E7-4850 v3 2.20GHz CPUs and 1TB memory.

First, we consider a dielectric sphere with a radius of $0.5m$. The sphere is decomposed into 4 sub-domains, as shown in Fig. 3. The dielectric constant ε_r of the sphere is increased from 2 to 16. The various parameters of the sphere are presented in Table I. In our following calculations, the radius of the sphere and the mesh size are consistent with this example. Since both surface electric and magnetic currents are unknown quantities, the total number of unknowns is twice the number of edges. The sphere is first simulated by the DG method with a block diagonal preconditioner. The $\theta\theta$-polarized bistatic RCS is calculated with the direction of an incident plane wave is $-z$ axis and the frequency is 300MHz. The iteration numbers of the DG method with BDP are listed in Table I. It can be seen that when the dielectric constant of the sphere is larger than 5, the iteration convergence speed becomes very poor. In some cases, the convergence cannot be achieved within 500, which is denoted as "no convergence (NC)" in Table I.

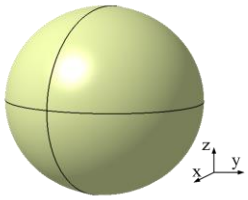

Fig. 3. The domain partitioning for the dielectric sphere

TABLE I: PARAMETERS OF THE DIELECTRIC SPHERE

ε_r	element size/ λ_0	Number of edges	Iteration
2	0.1	1,204	80
3	0.09	1,418	97
4	0.08	1,883	165
5	0.07	2,356	403
6	0.06	3,212	NC
8	0.05	4,648	411
10	0.045	5,804	329
12	0.04	7,176	358
14	0.035	9,540	NC
16	0.03	12,856	NC

Then we use the DG method with LTASP and the proposed DS-LTASP to calculate the sphere with a dielectric constant of 16. The value of the coefficient β in (16) and L in (20) are firstly set as 0.5 and $0.5\lambda_0/\sqrt{\varepsilon_r}$, respectively. The $\theta\theta$-polarized bistatic RCS in the xz-plane for this sphere are presented in Fig. 4. The numerical results agree well with the analytical Mie-series solution. The convergence histories of the GMRES solution are shown in Fig. 5. The DG method with LTASP and the DS-LTASP provide far less iterative numbers compared with the DG method with BDP.

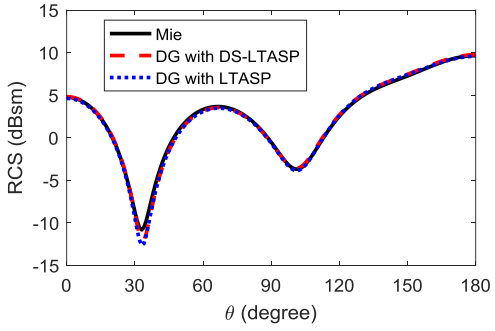

Fig. 4. $\theta\theta$ - polarized bistatic RCS of the sphere with a dielectric constant of 16.

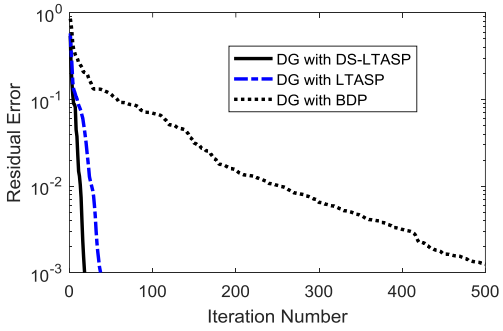

Fig. 5. Convergence histories for the sphere with a dielectric constant of 16 under different methods.

In order to investigate the effect of the interior penalty term, we change the value of the coefficient β in equation (16) and calculate the sphere with a dielectric constant of 16. The iteration numbers for different values of β are presented in Table II. It can be seen that when β is not zero, the value of β does not affect the number of iterations in a large range. The following numerical simulations set coefficient β as 0.5.

TABLE II
COMPARISON OF THE ITERATION NUMBER OF DIFFERENT β BY THE DG METHOD WITH LTASP AND DS-LTASP FOR THE DIELECTRIC SPHERE

β	0	0.5	1	5	10	20	50	100
LTASP	72	65	66	65	65	65	65	65
DS-LTASP	45	39	39	39	39	39	39	39

To study the impact of L to the efficiency and accuracy of the preconditioning solution, we compare the numerical performance of DG with DS-LTASP with different values of L. The results for the sphere with a dielectric constant of 16 are plotted in Fig. 6. The memory for PreC in Fig. 6 is the memory used for the analysis and factorization step of MUMPS for constructing the inverse matrix of the preconditioners. The relative error is defined as

$$e = \sqrt{\frac{\sum_{n=1}^{N}\left|\sigma_{cal}-\sigma_{Mie}\right|^2}{\sum_{n=1}^{N}\left|\sigma_{ref}\right|^2}} \qquad (21)$$

where σ_{cal} denotes the RCS computed with the numerical method, σ_{Mie} the analytical Mie-series solution, and N the number of observing angles. When L is very small, the iteration convergence of the solution is very poor. As L increases, the number of iterations decreases rapidly and then tends to keep stable. The memory used for preconditioner increases exponentially as the increase of L. When L is larger than the size of the lowest-level box of MLFMA, DS-LTASP is in fact the same as LTASP. The value of L has no effect on accuracy. Based on our results, we choose $L = 0.5\lambda_0/\sqrt{\varepsilon_r}$ in order to guarantee the efficiency of the solution.

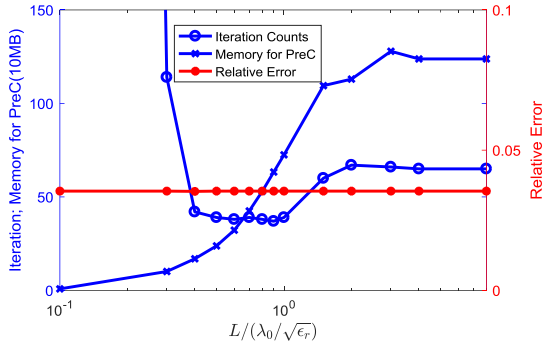

Fig. 6. The iteration numbers of the DG method with DS-LTASP, the memory used for constructing the preconditioner and the relative errors of RCS for the sphere with a dielectric constant of 16 as a function of L.

Then the numerical performance of the DG method with LTASP and DS-LTASP are compared for the spheres with various dielectric constants, as shown in Table III. The time and the memory for PreC in Table III are those for the analysis and factorization step of MUMPS for constructing the inverse matrix of the preconditioners. It can be seen that the CPU time and memory required by DS-LTASP are far less than that by LTASP, especially when the dielectric constant is large. Compared with the DG method with BDP, The iteration numbers of these two methods are much smaller. In addition, it can be observed that the DS-LTASP has a faster convergence speed than LTASP, which indicates that the sparse strategy of DS-LTASP is very effective. To intuitively show the sparsity of $\mathbf{P}^{sp}$, the matrix pattern of $\mathbf{V}^{NF(sp)}$ and $\mathbf{V}^{NF}$ (which are the upper left matrices of $\mathbf{P}^{sp}$ and $\mathbf{P}$, respectively) for the sphere with a dielectric constant of 16 are compared in Fig. 7.

TABLE III
COMPARISON OF THE NUMERICAL PERFORMANCE OF THE DG METHOD WITH LTASP AND DS-LTASP FOR THE DIELECTRIC SPHERE

ε_r	Iteration		Time for PreC(s)		Memory for PreC(MB)	
	DS-LTASP	LTASP	DS-LTASP	LTASP	DS-LTASP	LTASP
5	15	16	0.3	0.4	22	38
6	18	21	0.4	0.8	32	67
8	19	23	0.8	2	59	143
10	18	25	1	5	70	263
12	19	28	2	8	96	381
14	20	35	3	18	147	664
16	19	38	5	38	238	1,238

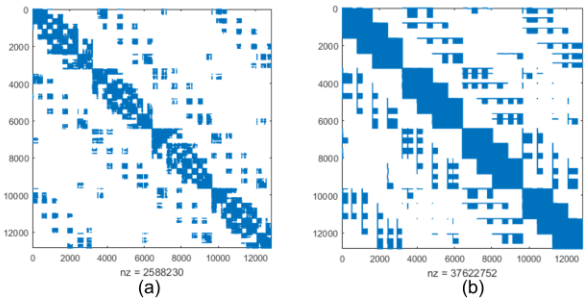

Fig. 7. The matrix pattern of $\mathbf{V}^{NF(sp)}$ and $\mathbf{V}^{NF}$ for the sphere with a dielectric constant of 16, nz represents the number of non-zero elements . (a) The matrix pattern of $\mathbf{V}^{NF(sp)}$, (b) The matrix pattern of $\mathbf{V}^{NF}$.

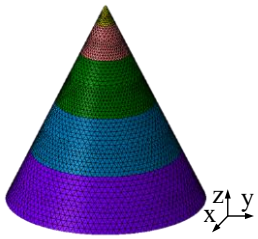

Fig. 8. Non-conformal surface discretization of a cone-shaped target with a dielectric constant of 16.

TABLE IV
COMPARISON OF THE NUMERICAL PERFORMANCE OF THE DG METHOD WITH LTASP AND DS-LTASP FOR THE DIELECTRIC CONE

ε_r	Iteration		Time for PreC(s)		Memory for PreC(MB)	
	DS-LTASP	LTASP	DS-LTASP	LTASP	DS-LTASP	LTASP
5	33	27	1.5	2.7	83	175
6	30	27	2.3	6.1	105	303
8	65	102	4.3	13.0	166	548
10	53	61	4.5	23.2	206	841
12	48	55	6.0	37.2	240	1183
14	95	80	7.0	62.3	295	1660
16	65	82	9.6	96.4	362	2276

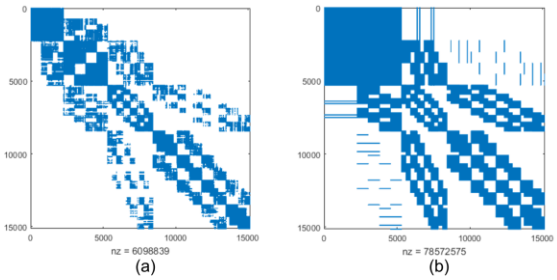

Fig. 9. The matrix pattern of $\mathbf{V}^{\mathrm{NF(sp)}}$ and $\mathbf{V}^{\mathrm{NF}}$ for the cone with a dielectric constant of 16. (a) The matrix pattern of $\mathbf{V}^{\mathrm{NF(sp)}}$, (b) The matrix pattern of $\mathbf{V}^{\mathrm{NF}}$.

The numerical performance of the DG method with LTASP and the DS-LTASP are further compared for a cone-shaped object, which has muti-scale geometric features and non-conformal patches. The cone has a height of $1m$ and a bottom radius of $0.5m$. The dielectric constant of the cone is increased from 5.0 to 16.0. The body is illuminated by a plane wave with a frequency of 300 MHz propagating in $-z$ direction. The surface of the cone is decomposed into 5 sections. Different discretization sizes are used for different sections and the meshes between different sections are non-conformal. The mesh size is 10mm, 15mm, 20mm, 25mm, and 30mm from top to bottom when $\varepsilon_r = 16$, as shown in Fig. 8. For other values of ε_r, the mesh size is scaled with the medium wavelength accordingly. The $\theta\theta$-polarized bistatic RCS of the cone is calculated. The numerical performance of the DG method with LTASP and DS-LTASP are compared in Table IV. The matrix pattern of the upper left matrix of $\mathbf{P}^{\mathrm{sp}}$ and $\mathbf{P}$ for the cone with a dielectric constant of 16 are drawn in Fig. 9. It can be observed that the matrix of DS-LTASP is much sparser than that of LTASP. Thus the time and memory used for constructing the inverse matrix of DS-LTASP are much less than that of LTASP. As the dielectric constant becomes higher, the iteration number of the DG method with DS-LTASP keeps small and generally less than that of the solution with LTASP.

Then the iteration convergence speed of DS-LTASP for calculating the targets with different number of subdomains is tested. As shown in Fig. 10, the number of subdomains (M) of the sphere is increased from 4 to 56. The iteration numbers of DS-LTASP for calculating the spheres in Fig. 10 with a dielectric constant of 16 are shown in Table V. The iteration keeps almost constant with the increase of M.

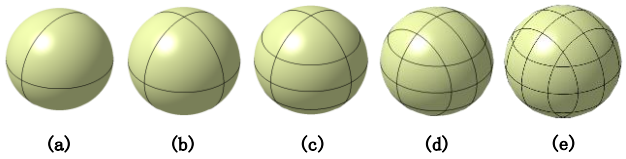

Fig. 10. Domain partitioning for the dielectric sphere. (a) M=4. (b) M=8. (c) M=16. (d) M=32. (e) M=56.

TABLE V
COMPARISON OF THE ITERATION NUMBERS OF THE DG METHOD WITH DS-LTASP FOR DIFFERENT DECOMPOSED SPHERES

M	4	8	16	32	56
Iteration	19	20	19	20	20

To demonstrate the capability of the DG method with DS-LTASP for targets with electrical large size, a sphere with 56 subdomains and dielectric constant of 16 is simulated under higher frequencies. The iteration numbers for the sphere under different frequencies are presented in Table VI. The time for DS-LTASP and the total solution time are compared in Fig. 11 as a function of the number of edges. It can be seen from Table VI and Fig. 11 that the DS-LTASP has a high iteration convergence speed to solve the high dielectric problem while costs the negligible CPU time compared with the total solution time.

TABLE VI
THE ITERATION NUMBERS OF THE DG METHOD WITH DS-LTASP FOR DIFFERENT PARAMETERS OF THE DIELECTRIC SPHERE

Freq (GHz)	Number of edges	Iteration
0.3	12,960	20
0.6	49,713	36
0.8	91,842	42
1.0	137,577	87
1.2	198,378	86
1.5	307,218	89
2.0	543,003	146

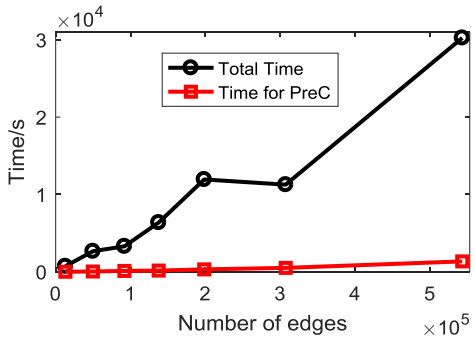

Fig. 11. Total solution time as a function of number of edges.

Finally, we calculate a dielectric four-rotor aircraft model with a dielectric constant of 10.0. The radius and the height of

the four-rotor aircraft are approximately 760mm and 120mm, respectively. The operating frequency is 1GHz, and the incident plane wave propagates along the –z direction. The surface of the model is divided into 9 parts. As drawn in Fig. 12, these parts are independently meshed with three different mesh sizes, which are 12mm, 8mm, 5mm. The total number of edges is 20,800. The bistatic RCS patterns are computed using the DG method with DS-LTASP and compared with the results obtained by the conventional CTF with MLFMA under the uniform conformal discretization with 70,551 edges. The results are in great agreement, as shown in Fig. 13. The conventional CTF requires a much large number of iterations compared with the proposed DG approach, as shown in Fig. 14.

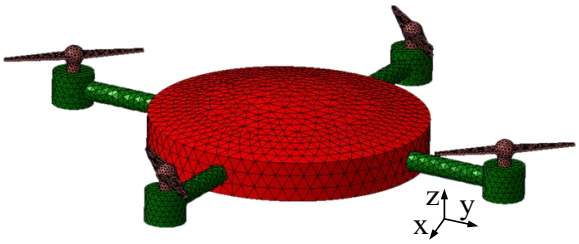

Fig. 12. Non-conformal surface discretization of a four-rotor aircraft model.

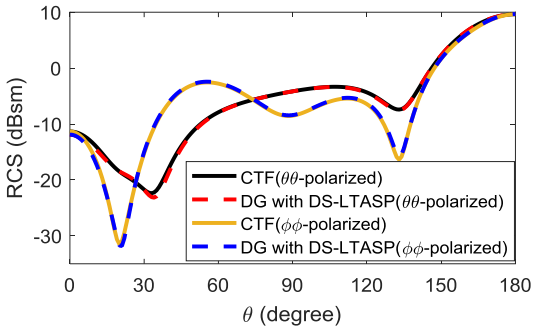

Fig. 13 The $\theta\theta$ -and $\phi\phi$ -polarized bistatic RCS of the four-rotor aircraft model.

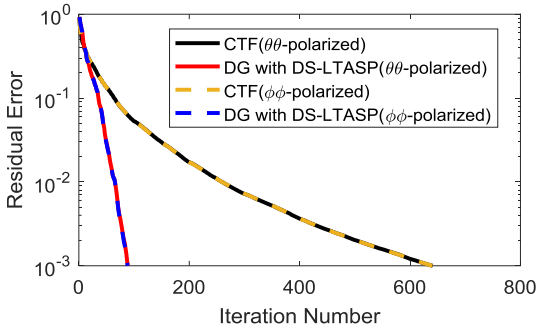

Fig. 14. Convergence histories for the four-rotor aircraft model under different methods.

V. Conclusion

A DG method of surface integral solution for homogeneous bodies with a high dielectric constant is studied in this communication. An efficient preconditioner DS-LTASP is designed in this solution. Based on the LTASP for CTF equations, the strong and critical interactions are effectively screened and a sparse preconditioning matrix is obtained. The cost of constructing the preconditioner is considerably reduced. Numerical experiments verify that the DS-LTASP has a better numerical performance in saving computing resources and improving convergence speed compared with LTASP. It is demonstrated that the proposed DG method with DS-LTASP has great capability for high dielectric multi-scale problems. The difficulty of the DG method with BDP for high dielectric constant cases is effectively solved.

References

[1] Z. Peng and J.-F. Lee, "Non-conformal domain decomposition method with second-order transmission conditions for time-harmonic electromagnetics," *J. Comput. Phys*., vol. 229, no. 16, pp. 5615–5629, Aug. 2010.

[2] M. F. Xue and J. M. Jin, "Nonconformal FETI-DP methods for large-scale electromagnetic simulation," *IEEE Trans. Antennas Propag*., vol. 60, no. 9, pp. 4291-4304, Sep. 2012.

[3] M.-L. Yang, H.-W. Gao, and X.-Q. Sheng, "Parallel domain decomposition-based algorithm of hybrid FE-BI-MLFMA method for 3-D scattering by large inhomogeneous objects," *IEEE Trans. Antennas Propag*., vol. 61, no. 9, pp. 4675–4684, Sep. 2013.

[4] H.-W. Gao, M.-L. Yang, and X.-Q. Sheng, "Nonconformal FETI-DP domain decomposition methods for FE-BI-MLFMA," *IEEE Trans. Antennas Propag.*, vol. 64, no. 8, pp. 3521–3532, Aug. 2016.

[5] H.-W. Gao, Z. Peng, and X.-Q. Sheng, "A geometry-aware domain decomposition preconditioning for hybrid finite element-boundary integral method," *IEEE Trans. Antennas Propag*., vol. 65, no. 4, pp. 1875–1885, Apr. 2017.

[6] M.-K. Li and W. C. Chew, "Wave-field interaction with complex structures using equivalence principle algorithm," *IEEE Trans. Antennas Propag.*, vol. 55, no. 1, pp. 130–138, Jan. 2007.

[7] M.-K. Li and W. C. Chew, "Multiscale simulation of complex structures using equivalence principle algorithm with high-order field point sampling scheme," *IEEE Trans. Antennas Propag.*, vol. 56, no. 8, pp. 2389–2397, Aug. 2008.

[8] Z. Peng, X.-C. Wang, and J.-F. Lee, "Integral equation based domain decomposition method for solving electromagnetic wave scattering from non-penetrable objects," *IEEE Trans. Antennas Propag.*, vol. 59, no. 9, pp. 3328–3338, Sep. 2011.

[9] Z. Peng, K.-H. Lim, and J.-F. Lee, "Computations of Electromagnetic wave scattering from penetrable composite targets using a surface integral equation method with multiple traces," *IEEE Trans. Antennas Propag.*, vol. 61, no. 1, pp. 256–270, Jan. 2013.

[10] Z. Peng, K.-H. Lim, and J.-F. Lee, "A discontinuous Galerkin surface integral equation method for electromagnetic wave scattering from nonpenetrable targets," *IEEE Trans. Antennas Propag.,* vol. 61, no. 7, pp. 3617–3628, July 2013.

[11] Z. Peng, R. Hiptmair, Y. Shao, and B. MacKie-Mason, "Domain decomposition preconditioning for surface integral equations in solving challenging electromagnetic scatteriing problems," *IEEE Trans. Antennas Propag.,* vol. 64, no. 1, pp. 210-223, Jan. 2016

[12] L.-M. Zhang and X.-Q. Sheng, "A discontinuous Galerkin volume integral equation method for scattering from inhomogeneous objects," *IEEE Trans. Antennas Propag.*, vol. 63, no.12, pp. 5661-5667, Dec. 2015.

[13] L.-M. Zhang and X.-Q. Sheng, "Discontinuous Galerkin volume Integral equation solution of scattering from inhomogeneous dielectric objects by using the SWG basis function," *IEEE Trans. Antennas Propag.*, vol. 65, no. 3, pp. 1500–1504, March 2017.

[14] B.-B. Kong and X.-Q. Sheng, "A Discontinuous Galerkin Surface Integral Equation Method for Scattering from Multi-Scale Homogeneous Objects," *IEEE Trans. Antennas Propag*, vol.66, no.4, pp. 1937–1946, Apr. 2018.

[15] X. Wang, "A domain decomposition method for analysis of threedimensional large-scale electromagnetic compatibility problems," Ph.D. dissertation, Ohio State Univ., Columbus, OH, USA, 2012

[16] T. Malas and L. Gürel, "Schur complement preconditioners for surface integral-equation formulations of dielectric problems solved with the multilevel fast multipole algorithm," *SIAM Journal on Scientific Computing*, Vol. 33, No. 5, 2440-67, 2011.